

Coarse-grained modeling of multiphase interactions at microscale

Pengyu Huang, Luming Shen, Yixiang Gan, Giang D. Nguyen, Abbas El-Zein, and Federico Maggi

Citation: [The Journal of Chemical Physics](#) **149**, 124505 (2018); doi: 10.1063/1.5038903

View online: <https://doi.org/10.1063/1.5038903>

View Table of Contents: <http://aip.scitation.org/toc/jcp/149/12>

Published by the [American Institute of Physics](#)

Articles you may be interested in

[Statistical field theory for polar fluids](#)

The Journal of Chemical Physics **149**, 124108 (2018); 10.1063/1.5046511

[Influence of solvent quality on conformations of crowded polymers](#)

The Journal of Chemical Physics **149**, 124901 (2018); 10.1063/1.5043434

[Perspective: Dissipative particle dynamics](#)

The Journal of Chemical Physics **146**, 150901 (2017); 10.1063/1.4979514

[A coherent derivation of the Ewald summation for arbitrary orders of multipoles: The self-terms](#)

The Journal of Chemical Physics **149**, 124103 (2018); 10.1063/1.5044541

[Communication: Adaptive boundaries in multiscale simulations](#)

The Journal of Chemical Physics **148**, 141104 (2018); 10.1063/1.5025826

[MonteCoffee: A programmable kinetic Monte Carlo framework](#)

The Journal of Chemical Physics **149**, 114101 (2018); 10.1063/1.5046635

PHYSICS TODAY

WHITEPAPERS

ADVANCED LIGHT CURE ADHESIVES

READ NOW

Take a closer look at what these
environmentally friendly adhesive
systems can do

PRESENTED BY



Coarse-grained modeling of multiphase interactions at microscale

Pengyu Huang,¹ Luming Shen,^{1,a)} Yixiang Gan,¹ Giang D. Nguyen,² Abbas El-Zein,¹ and Federico Maggi¹

¹School of Civil Engineering, The University of Sydney, Sydney, NSW 2006, Australia

²School of Civil, Environmental and Mining Engineering, The University of Adelaide, Adelaide, SA 5005, Australia

(Received 7 May 2018; accepted 11 September 2018; published online 26 September 2018)

The objective of this study is to develop and test a coarse-grained molecular dynamics framework to model microscale multiphase systems with different inter-particle interactions and recover emerging thermodynamic and mechanical properties at the microscale. A water-vapor model and a fused silica model are developed to demonstrate the capability of our framework. The former can reproduce the water density and surface tension over a wide range of temperatures; the latter can reproduce experimental density, tensile strength, and Young's modulus of fused silica. Therefore, the deformable solid model is implemented in the proposed framework. Validations of spatial scaling methods for solid, liquid, and multiphase systems suggest that the proposed framework can be calibrated at an arbitrary microscale and used at a different length scale without recalibration. Different values of wettability for a solid-liquid-vapor system that is characterized by the contact angle can be achieved by changing the solid-liquid inter-particle potential. Thanks to these features, the proposed coarse-grained molecular dynamics framework can potentially find applications in modeling systems in which multiple phases coexist and have substantial interactions. *Published by AIP Publishing.*

<https://doi.org/10.1063/1.5038903>

I. INTRODUCTION

It is critical to understand and predict the mechanical and hydraulic behavior of partially saturated porous media under various loading conditions given its importance in many applications in civil and mining engineering, petroleum engineering, earthquake engineering, and hydrogeological sciences. The dynamics of partially saturated porous media have been studied with experimental techniques, suggesting that the effect of pore fluid can be crucial in the response of geo-materials under loading.¹ However, it is hard to quantify the effect of pore fluid on the solid skeleton experimentally. For example, it is very challenging to measure the pore water pressure in partially saturated porous media,² which can significantly affect solid crushing.^{3,4} To better quantify the effect of pore fluid on the response of porous media to stresses, numerical simulations can be an effective way to study the multiphase interaction quantitatively for a better understanding of the hydro-mechanical coupling in partially saturated porous media.

Partially saturated porous media exhibit multiphase interactions across multiple scales. At the macroscopic scale, the representative element volume of partially saturated porous media is assumed to be homogeneous as commonly found in continuum constitutive models implemented in finite element methods.^{5–7} However, the assumptions on homogeneity in these continuum models do not hold at the microscale of

materials made of discrete and heterogeneous grains with unevenly distributed pores filled with liquid and/or air. In addition, the mesh in finite element methods usually has difficulties in handling large deformations of the representative volume element due to severe mesh distortion, making the simulation of grain crushing difficult. In this sense, a particle-based method can be more suitable for modeling partially saturated porous media at the microscopic scales. So far, several methods have been developed to model multiphase interactions, especially for multiphase fluids and fluid-solid interactions. The Lattice Boltzmann Method (LBM),⁸ dissipative particle dynamics (DPD),⁹ smoothed particle hydrodynamics (SPH),¹⁰ and grid-based computational fluid dynamics coupled with an interface tracking model such as the volume-of-fluid (VOF) method¹¹ have been used for simulating multiphase flows. Some of these methods, such as the LBM and VOF method, can be coupled with the discrete element method (DEM) to model transport of solid particles.^{8,12} However, in these methods, solids are generally non-deformable and thus grain deformation or crushing cannot be effectively modeled.

At the atomic scale, molecular dynamics (MD) methods are suitable for modeling multiphase systems, where materials and phases can be described by atoms and molecules.¹³ However, carrying out MD simulations at microscopic scales can be extremely costly due to the need of a very large number of atoms and molecules and small step sizes for time integration. To model multiphase interactions with deformable solid at the microscopic scale, therefore, a particle-based coarse-grained approach is proposed in this study. This idea follows from coarse-grained molecular dynamics (CGMD), which uses one

^{a)}Author to whom correspondence should be addressed: luming.shen@sydney.edu.au. Tel.: +61-2-93512126. Fax: +61-2-93513343.

particle to represent a group of atoms or molecules in order to reduce the degrees of freedom of the system.

In general, there are two main groups of coarse-grained (CG) methods: (1) the bottom-up method, where the CG potential function is derived from the information retrieved from all-atomistic simulations; (2) the top-down method, where an imposed potential function is selected, and the parameters are optimized to meet the targeted macroscopic properties. For the bottom-up method, one approach is to estimate the pair potential derived from the resultant forces of a cluster of MD particles and the trajectories using a multiscale coarse-graining method (MS-CG) or a force matching (FM) method.¹⁴ The CG potential force field can also be derived from the MD particle distribution using iterative Boltzmann inversion (IBI).¹⁵ However, the CG potential constructed from the bottom-up method at one thermodynamic state may not be suitable for recovering properties at a different thermodynamic state, and the derivation of the density-dependent or temperature-dependent CG potential would be required.¹⁶

The top-down method aims to fit the thermodynamic quantities to experimental observations by adjusting the parameters of a proposed potential model. There are several CG models for fluids that map small numbers of molecules into one CG particle using mathematical potential functions such as Lennard-Jones (LJ), Mie, and Morse potential.^{17–19} By contrast, the DPD and many-body dissipative particle dynamics (MDPD) are able to map a large number of molecules (e.g., $\sim 10^6$ water molecules or above) into one particle by matching the relevant properties against experimental data.^{20,21} In addition, the scaling method for DPD was proposed to scale the DPD system to any desired length scale by Füchslin *et al.*²² This method has also been applied to the MDPD system recently.²⁰ While compressibility of the modeled material is conserved during scaling from one length scale to another, the surface tension reproduced by the MDPD model is not conserved.²⁰

The original DPD force field leads to an equation of state where pressure is a quadratic function of density.²³ The MDPD was first introduced by Pagonabarraga and Frenkel²⁴ as an extension to DPD by using the density-dependent repulsive force, to have more options for the equation of state. MDPD was later improved by Warren²⁵ to model liquid-vapor interfaces, by including the attractive and repulsive forces at different ranges. The studies and developments of MDPD are an active research area, especially for multiphase interactions. Ghoufi and Malfreyt²⁶ have reported that the MDPD method is able to reproduce the experimental density, surface tension, and compressibility of water by calibrating one of the MDPD parameters to fit the surface tension at 298 K. In their studies, one MDPD particle represented three water molecules and a top-down coarse-graining method was used. Arienti *et al.*²⁰ also have used a set of simple scaling relations which links the MDPD model from a dimensionless system to dimensional system by reproducing the experimental density, surface tension, and viscosity properties of various fluids. Goujon *et al.*²⁷ studied the finite-size effects of the surface area on surface tension for several coarse-grained models, including the MDPD water model reported by Ghoufi and Malfreyt.²⁶ They showed that there is a weak dependence of the surface tension on the

surface area for the MDPD water model. Recent studies commonly adopt the MDPD force field for the MDPD solid-liquid interactions and control the wettability by adjusting the parameter of attractive forces between solid and liquid particles.²⁸ Other solid-liquid interaction models which use a force function with attractive and repulsive forces are also possible.²⁰ As a result, the MDPD droplet on a solid substrate can also be modeled.²⁹ The coalescence of water droplets on the water surface was also studied using the MDPD model.³⁰

In this paper, the top-down method is used to map many molecules into one particle without running the full atomistic simulations, which are not affordable at the micro-length scales in most situations. A framework based on the CGMD is developed within LAMMPS.³¹ This proposed framework combines MDPD, the Morse potential function, and the Lennard-Jones potential function to describe the multiphase interactions of the solid-liquid-vapor system with solid being modeled deformable. Specifically, MDPD and the Morse potential function will be used to describe the liquid-liquid (or liquid-vapor) and solid-solid inter-particle interactions, respectively, while the solid-liquid inter-particle interaction will be modeled using the Lennard-Jones potential function.

The capability of the framework is demonstrated by calibrating the simulated physical quantities against experimentally measured values of (1) the density and surface tension of water at room temperature, and the changes in water surface tension against the temperature for the MDPD liquid-vapor model; and (2) the density, Young's modulus, and tensile strength of fused silica for the Morse-potential solid model. For solid-liquid-vapor interactions, water droplets on a solid substrate with different wetting ability are modeled, resulting in different contact angles. The scaling method in Ref. 22 is applied to maintain the bulk properties of the solid model but modified to maintain the surface tension of the MDPD liquid-vapor model during scaling. In addition, the scaling method is also extended to the multiphase system for modeling microscopic systems of different sizes without recalibration of model parameters.

The remaining sections of the paper are organized as follows. Section II presents the potential functions used for the inter-particle interactions (Sec. II A), parameters calibration for the liquid-vapor and solid models (Sec. II B), the scaling methods for liquid-vapor, solid, and solid-liquid-vapor systems (Sec. II C), numerical validation for liquid-vapor and solid models, and the solid-liquid-vapor system applications used in the simulations (Sec. II D). Section III describes and discusses the results of the numerical validation and applications. Section IV presents the conclusions of this work. Appendixes A–E report the details of all simulations carried out in this work.

II. METHODS

A. Potential functions for inter-particle interactions

Under the proposed coarse-grained framework, all phases are discretized and modeled by the coarse-grained particles. The motions of all particles obey the laws of Newtonian mechanics. The potential functions for inter-particle interactions are described in this section.

The interaction between liquid-liquid or liquid-vapor particles is described by MDPD forces. Only the conservative part of the MDPD interaction is adopted here; its dissipative and random forces that act as a thermostat in DPD are not included. The DPD thermostat indeed can conserve momentum locally and hence preserve hydrodynamics.³⁰ While the DPD thermostat has been used for fluid and hydrodynamics modeling, the Nosé-Hoover chain thermostat^{13,32,33} has been applied successfully in both solid and liquid models, as well as the multiphase system at the atomistic level. Since our proposed model also includes the modeling of deformable solid grains, the Nosé-Hoover chain thermostat is used in our framework for temperature control. The conservative force \mathbf{F}_{ij} on the i th particle due to the j th particle is expressed as²⁵

$$\mathbf{F}_{ij} = Aw_c(r_{ij})\mathbf{e}_{ij} + B(\rho_i + \rho_j)w_d(r_{ij})\mathbf{e}_{ij}, \quad (1)$$

where A and B are parameters of the attractive and repulsive forces, respectively; r_{ij} is the distance between the i th and the j th particles; \mathbf{e}_{ij} is the unit vector pointing from the j th particle to the i th particle; $w_c(r_{ij})$ and $w_d(r_{ij})$ are the weight functions defined as

$$w_c(r_{ij}) = \begin{cases} 1 - \frac{r_{ij}}{r_c}, & r_{ij} \leq r_c \\ 0, & r_{ij} > r_c, \end{cases} \quad (2)$$

$$w_d(r_{ij}) = \begin{cases} 1 - \frac{r_{ij}}{r_d}, & r_{ij} \leq r_d \\ 0, & r_{ij} > r_d, \end{cases} \quad (3)$$

where r_c and r_d are the cutoff distances for the attractive and repulsive forces, respectively. r_c is greater than r_d to recover the attractive force at the surface. The weighted local density of the i th particle, ρ_i , is calculated as the sum of the weight function w_p toward its neighbor particles up to the cutoff radius r_d ,

$$\rho_i = \sum_{j \neq i} w_p = \sum_{j \neq i} \frac{15}{2\pi r_d^3} \left(1 - \frac{r_{ij}}{r_d}\right)^2, \quad r_{ij} \leq r_d. \quad (4)$$

The force on the i th particle due to the j th particle calculated in the embedded atom method (EAM)³⁴ has a similar structure as \mathbf{F}_{ij} in Eq. (1), where the first term of Eq. (1) is a pairwise force and the second term of Eq. (1) is related to the local density functions. To implement the MDPD into molecular dynamics simulator LAMMPS, the MDPD potential energy of the i th particle can be calculated using Eq. (1) and written in the form of the EAM potential,

$$u_i = \frac{1}{2} \sum_{j \neq i} \frac{Ar_c}{2} w_c(r_{ij})^2 + \frac{\pi r_d^4}{30} B \rho_i^2, \quad (5)$$

where u_i is the potential energy of the i th particle.

To model the interaction between solid particles, a pairwise Morse potential function with a cutoff distance $r_{ss,cut}$ is used,

$$u_{ss} = \begin{cases} D_o [\exp(-2\alpha(r_{ss} - r_o)) - 2 \exp(-\alpha(r_{ss} - r_o))], & r_{ss} < r_{ss,cut} \\ 0, & r_{ss} \geq r_{ss,cut}, \end{cases} \quad (6)$$

where u_{ss} is the potential energy between two solid particles and r_{ss} is their relative distance; D_o and r_o are the depth of the potential well (minimum energy for the Morse potential) and the location of the well, respectively; the parameter α controls the curvature of the potential well at r_o . Since the Morse potential function has three parameters D_o , r_o , and α , it can be fitted against the three mechanical properties, i.e., density, Young's modulus, and tensile strength of a particular solid material.

The interaction between solid and liquid particles in a full-atom MD scheme has commonly been modeled using the Lennard-Jones (LJ) potential, which is also adopted in our CG model. The potential energy u_{sl} between a liquid particle and a solid particle, separated by a distance r_{sl} , is given by

$$u_{sl} = \begin{cases} 4\varepsilon_{sl} \left[\left(\frac{\sigma_{sl}}{r_{sl}} \right)^{12} - \left(\frac{\sigma_{sl}}{r_{sl}} \right)^6 \right], & r_{sl} < r_{sl,cut} \\ 0, & r_{sl} \geq r_{sl,cut}, \end{cases} \quad (7)$$

where ε_{sl} and σ_{sl} are the potential well and distance for the LJ potential, respectively. The LJ potential has a minimum energy at the distance of $2^{1/6}\sigma_{sl}$ between a liquid and a solid particle. While different σ_{sl} values can be used in Eq. (7), we estimate

σ_{sl} as the arithmetic mean,

$$\sigma_{sl} = 2^{-\frac{1}{6}} \left(\frac{r_{mdpd} + r_o}{2} \right), \quad (8)$$

where r_o is the location of the minimum energy in the Morse potential and r_{mdpd} is estimated from the distance of the first peak in the pair distribution function of the liquid model. Adjusting ε_{sl} can easily lead to different levels of solid-liquid interaction and will result in various degrees of wettability for the solid-liquid-vapor system, i.e., different contact angles.

Simulations are run in dimensionless units in the MDPD. As all MDPD particles have the same particle mass m_{mdpd} and the cut-off distance for attractive force r_c , both m_{mdpd} and r_c are equal to the unity in dimensionless unit, i.e., the unit of mass $m_{mdpd}^* = 1$ and the unit of length $\sigma_{mdpd}^* = r_c^* = 1$. In addition, the dimensionless MDPD parameters [Eq. (5)] can be expressed in terms of the fundamental units of energy $\varepsilon_{mdpd}^* = 1$ and distance σ_{mdpd} as $A^* = A\sigma_{mdpd}/\varepsilon_{mdpd}$, $B^* = B/(\varepsilon_{mdpd}\sigma_{mdpd}^2)$, $r_c^* = r_c/\sigma_{mdpd} = 1$, and $r_d^* = r_d/\sigma_{mdpd}$. Note that a variable with the asterisk represents a dimensionless quantity. Consequently, the dimensionless properties of the MDPD system are expressed in terms of the fundamental

units as density $\rho^* = (N/V)\sigma_{\text{mdpd}}^3$, length $L^* = L/\sigma_{\text{mdpd}}$, surface tension $\gamma^* = \gamma(\sigma_{\text{mdpd}}^2/\varepsilon_{\text{mdpd}})$, pressure $P^* = P(\sigma_{\text{mdpd}}^3/\varepsilon_{\text{mdpd}})^{1/2}$, and time $t^* = t(\varepsilon_{\text{mdpd}}/m_{\text{mdpd}}\sigma_{\text{mdpd}}^2)^{1/2}$. Note that N is the number of particles and V is the volume of the system.

B. Methods of parameter calibration

The calibration of the liquid-vapor MDPD model parameters involves an iteration process, as explained next. The MDPD parameters are calibrated against experimental density and surface tension at room temperature, as well as the surface tension over a large range of temperatures. Since both MDPD parameters A^* and B^* are related to the energy unit $\varepsilon_{\text{mdpd}}$, we can keep one parameter as invariant and vary the other. Here, we choose $A^* = -40$ and try to determine B^* . For r_c^* and r_d^* , we set $r_d^* = 0.75$ and $r_c^* = 1$ which have been used in earlier studies.^{20,26} Therefore, B^* is the only unknown. To fit the model of liquid phase against the surface tension at different temperatures, we define the reference dimensionless room temperature T_{room}^* by calculating the melting temperature T_m^* at atmospheric pressure $P_{1\text{atm}}^*$. T_m^* is calculated using direct solid-liquid coexistence simulation (see Appendix A) for the MDPD model with a given set of MDPD parameters at $P_{1\text{atm}}^*$. Therefore, $T_{\text{room}}^*(T_m^*)$ is a function of T_m^* with $T_{\text{room}} = 293.15$ K,

$$T_{\text{room}}^*(T_m^*) = \frac{T_{\text{room}}}{T_m} T_m^*, \quad (9)$$

where T_m is the experimental melting temperature at atmospheric pressure of the liquid. Since the MDPD model is calibrated against the liquid properties of water, $T_m = 273.15$ K is used.

For a given set of parameters (A^* , B^* , r_c^* , and r_d^*), both $\rho^*(T^*)$ and $\gamma^*(T^*)$ depend on T^* and their values can be calculated from the liquid-vapor interface simulations in the canonical ensemble (see Appendix B). When $T_{\text{room}}^*(T_m^*)$ is calculated, both $\rho^*(T_{\text{room}}^*(T_m^*))$ and $\gamma^*(T_{\text{room}}^*(T_m^*))$ are used to match the experimental density ρ_{exp} and surface tension γ_{exp} of the liquid at room temperature by calculating the values of the fundamental units. The real particle mass m_{mdpd}

depends on ρ_{exp} , the number of particles N used for modeling liquid phase, and the simulated liquid volume V ,

$$m_{\text{mdpd}} = \rho_{\text{exp}} V/N. \quad (10)$$

Then, the values of σ_{mdpd} and $\varepsilon_{\text{mdpd}}$ can be calculated from ρ_{exp} and γ_{exp} at a room temperature,

$$\sigma_{\text{mdpd}}(T_{\text{room}}^*(T_m^*)) = \left(m_{\text{mdpd}} \left(\frac{\rho^*(T_{\text{room}}^*(T_m^*))}{\rho_{\text{exp}}} \right) \right)^{\frac{1}{3}}, \quad (11)$$

$$\varepsilon_{\text{mdpd}}(T_{\text{room}}^*(T_m^*)) = \sigma_{\text{mdpd}}^2 \left(\frac{\gamma_{\text{exp}}}{\gamma^*(T_{\text{room}}^*(T_m^*))} \right). \quad (12)$$

The dimensionless atmospheric pressure $P_{1\text{atm}}^*$ is then calculated from $\sigma_{\text{mdpd}}(T_{\text{room}}^*(T_m^*))$ and $\varepsilon_{\text{mdpd}}(T_{\text{room}}^*(T_m^*))$, with $P_{1\text{atm}} = 101\,325$ Pa,

$$P_{1\text{atm}}^*(T_m^*) = P_{1\text{atm}} \frac{\sigma_{\text{mdpd}}^3(T_{\text{room}}^*(T_m^*))}{\varepsilon_{\text{mdpd}}(T_{\text{room}}^*(T_m^*))}. \quad (13)$$

Because the value of $P_{1\text{atm}}^*(T_m^*)$ can affect the calculation of T_m^* in the direct solid-liquid coexistence simulation, an iterative process is needed to calculate T_m^* (see Table I). We start from $P_0^* = 0$ to calculate $T_{0,m}^*$ for the initial value (the first subscript i is the i th iteration), since the vapor pressure is relatively small in the liquid-vapor system at low T^* . If $T_{1,\text{room}}^* < T_{0,m}^*$, the set of parameters is rejected because it would not be physically sound to simulate a liquid-vapor system at $T^* < T_m^*$. After T_m^* converges, T_{room}^* is also defined for each set of parameters [Eq. (9)] and the values of σ_{mdpd} and $\varepsilon_{\text{mdpd}}$ can be calculated [Eqs. (11) and (12)]. Since only the parameter B^* is unknown, $\gamma^*(T^*)$ calculated at different T^* for each B^* can be converted to dimensional values $\gamma(T)$ as $\gamma(T) = \gamma^*(T^*) \varepsilon_{\text{mdpd}}/\sigma_{\text{mdpd}}^2$ and $T = T^*(T_m/T_m^*)$. Hence, B^* is calibrated by fitting the calculated $\gamma(T)$ against the experimental value $\gamma_{\text{exp}}(T)$ at different T .

In the solid model, a trial and error heuristic search is used to calibrate the parameters of the Morse potential function D_o , r_o , and α against the experimental density, tensile strength, and Young's modulus of the fused silica in Ref. 35. The calculations of simulated density, tensile strength, and Young's modulus for the solid model are reported in Appendix D.

TABLE I. The algorithm of the iteration process for determining T_m^* for a given set of parameters.

Step no.	Description
1	For a given set of parameters (A^* , B^* , r_c^* , and r_d^*), calculate $T_{i,m}^*$ with $P_0^* = 0$ from the direct solid-liquid coexistence simulation (see Appendix A), starting from iteration $i = 0$
2	Calculate $T_{i,\text{room}}^*$ with $T_{i,m}^*$ using Eq. (9)
3	Compute ρ_i^* and γ_i^* from the liquid-vapor interface simulations using $T_{i,\text{room}}^*$ from Step 2 (see Appendix B)
4	Compute $\sigma_{i,\text{mdpd}}$ and $\varepsilon_{i,\text{mdpd}}$ using Eqs. (11) and (12) with $\rho_i^*(T_{i,\text{room}}^*)$ and $\gamma_i^*(T_{i,\text{room}}^*)$ from Step 3
5	Calculate $P_{i,1\text{atm}}^*$ with $\sigma_{i,\text{mdpd}}$ and $\varepsilon_{i,\text{mdpd}}$ from Step 4 using Eq. (13)
6	$i = i + 1$
7	Calculate $T_{i,m}^*$ with $P_{i-1,1\text{atm}}^*$ (calculated in Step 5) from the direct solid-liquid coexistence simulation (see Appendix A)
8	Repeat Step 2 to Step 7 until $ T_{i,m}^* - T_{i-1,m}^* /T_{i,m}^* \leq 0.5\%$, and $T_{i-1,m}^*$ is selected as the final T_m^* ; stop if $T_{1,\text{room}}^* \leq T_{0,m}^*$ and repeat from Step 1 by choosing a new set of parameters

C. Scaling methods

Füchsli *et al.*²² proposed a set of scaling relations to determine the DPD parameters from one scale and apply them to another scale. The main concept of the scaling method in Ref. 22 is illustrated in Fig. 1 for a 2D system. A 16-particle system [Fig. 1(a)] is scaled to a 4-particle system [Fig. 1(b)] by mapping 4 particles into one large particle and maintaining the same system size. The radius of particle interaction was also scaled accordingly (Fig. 1). Both systems can be converted from dimensionless systems [Fig. 1(c)] and the scaling relations are used to maintain the desired physical quantities. Here the scaling factor $\phi = N/N'$ is introduced, where N and N' are the two different particle numbers in the two systems of the same size. For example, $\phi = N/N' = 4$ for the scaling of the systems in Figs. 1(a) and 1(b), with $N = 16$ and $N' = 4$, respectively. The scaling relations of the fundamental units for a 3D system are listed as: the mass unit $m' = \phi m$, the energy unit $\varepsilon' = \phi \varepsilon$, and the length unit $\sigma' = \phi^{1/3} \sigma$, according to the method of Füchsli *et al.*²² where the “prime” indicates quantities in the N' system after scaling. The parameters and relevant physical quantities after scaling can then be calculated with the fundamental units.

The scaling method of Füchsli *et al.*²² maintains the bulk properties such as compressibility under the assumption of no phase transition during compression, while the interfacial properties such as surface tension are not necessarily conserved during scaling. We here provide an alternative way of deriving the scaling relations to maintain the surface tension quantity for the liquid-vapor system. The relationship between the dimensional compressibility κ and the dimensionless compressibility κ^* is expressed as $\kappa = \kappa^*(\sigma^3/\varepsilon)$. The dimensional compressibility after scaling κ' is calculated as $\kappa' = \kappa^*(\sigma'^3/\varepsilon') = \kappa^*((\phi^{1/3}\sigma)^3/\varepsilon') = \kappa^*(\phi\sigma^3/\varepsilon')$, with $\sigma' = \phi^{1/3}\sigma$. For the two systems before and after scaling to have the same compressibility, i.e., $\kappa = \kappa'$, equation $\varepsilon' = \phi\varepsilon$ must hold. Similarly, the surface tension before scaling is expressed as $\gamma = \gamma^*(\varepsilon/\sigma^2)$ and the surface tension after scaling is expressed as $\gamma' = \gamma^*(\varepsilon'/\sigma'^2) = \gamma^*(\varepsilon'/\phi^{2/3}\sigma^2)$, with $\sigma' = \phi^{1/3}\sigma$. Hence, $\varepsilon' = \phi^{2/3}\varepsilon$ is required

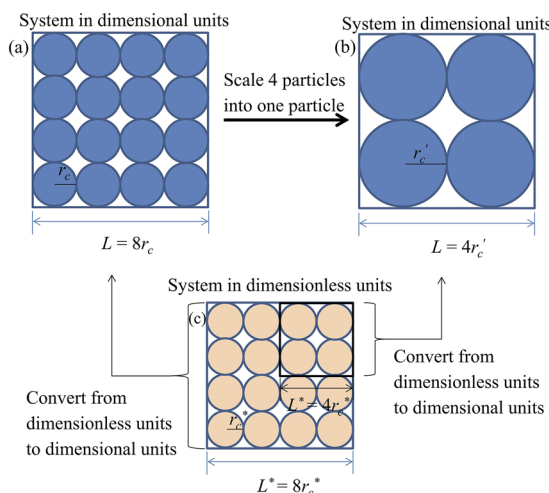


FIG. 1. The schematic plot of the scaling method by Füchsli *et al.*²² Reproduced with permission from Füchsli *et al.*, J. Chem. Phys. **130**, 214102 (2009). Copyright 2009 AIP Publishing LLC.

to have $\gamma' = \gamma$. This also explains why $\gamma' = \phi^{1/3}\gamma$ has been found when $\varepsilon' = \phi\varepsilon$ was used in the MDPD simulation as in Ref. 20, as $\gamma' = \gamma^*(\varepsilon'/\sigma'^2) = \gamma^*(\varepsilon/\sigma^2)\phi^{1/3} = \phi^{1/3}\gamma$. N' and N should be large enough to avoid the finite size effect in order to make the scaling relations valid. It should be noted that the surface tension is conserved with $\varepsilon' = \phi^{2/3}\varepsilon$ during our proposed scaling process, while the compressibility of the liquid is not conserved. Since the pressure of the vapor particles and the pressure induced from the curved surfaces of the droplets are relatively small, the change in compressibility would not affect liquid density much. The liquid density difference between the two simulated droplets with the scaling factors for the liquid-vapor model $\phi_{lv} = 1$ and $\phi_{lv}' = 1/64$ is within 0.5% at room temperature, as shown in Sec. III C, which is quite acceptable. On the other hand, the effect of surface tension on the microscale multiphase flow can be significant. Therefore, in order to maintain the surface tension instead of the compressibility, the modified scaling relations of the fundamental units for the MDPD liquid-vapor model are introduced as

$$m'_{\text{mdpd}} = \phi_{lv} m_{\text{mdpd}}, \quad (14)$$

$$\varepsilon'_{\text{mdpd}} = \phi_{lv}^{\frac{2}{3}} \varepsilon_{\text{mdpd}}, \quad (15)$$

$$\sigma'_{\text{mdpd}} = \phi_{lv}^{\frac{1}{3}} \sigma_{\text{mdpd}}, \quad (16)$$

where $\phi_{lv} = N_{lv}/N_{lv}'$ is the scaling factor for the liquid-vapor model and N_{lv} and N_{lv}' are the two numbers of liquid-vapor particles used to represent the same dimensional size. In addition, as the dimensional time is calculated as $t_{lv} = t_{lv}^*(m_{\text{mdpd}}\sigma_{\text{mdpd}}^2/\varepsilon_{\text{mdpd}})^{1/2}$, the scaled time can be expressed as $t_{lv}' = \phi_{lv}^{1/2} t_{lv}$ for the MDPD liquid-vapor model. The MDPD parameters after scaling are then calculated as

$$A' = \phi_{lv}^{\frac{1}{3}} A, \quad (17)$$

$$B' = \phi_{lv}^{\frac{4}{3}} B, \quad (18)$$

$$r'_c = \phi_{lv}^{\frac{1}{3}} r_c, \quad (19)$$

$$r'_d = \phi_{lv}^{\frac{1}{3}} r_d. \quad (20)$$

The fundamental units of the Morse-potential solid model are defined by using the particle mass m_s , the energy parameter D_o , and the distance parameter r_o . Therefore, to maintain the bulk properties of the solid model, the scaled particle mass and Morse potential parameters are calculated as

$$m'_s = \phi_s m_s, \quad (21)$$

$$D'_o = \phi_s D_o, \quad (22)$$

$$r'_o = \phi_s^{\frac{1}{3}} r_o, \quad (23)$$

$$\alpha' = \phi_s^{-\frac{1}{3}} \alpha, \quad (24)$$

where $\phi_s = N_s/N_s'$ is the scaling factor for the solid model, with N_s and N_s' as the two numbers of solid particles used to represent the same dimensional size. Hence, the scaled time for the solid model is $t_s' = \phi_s^{1/3} t_s$, as $t_s = t_s^*(m_s r_o^2/D_o)^{1/2}$.

To scale the liquid-vapor and solid model together in the same system, i.e., to maintain the same surface wettability during the scaling process, it requires scaling parameters of the LJ potential as well. Since different scaling relations are applied to the energy units for the liquid-vapor and solid systems, scaling in energy parameters of the LJ potential ε_{sl}^* requires that

TABLE II. The summary of the five simulation cases with the simulation setups being reported in Appendices A–E.

Case	Simulation	Potential model	Quantities calculated	Simulation purpose
1	Solid-liquid (Appendix A)	MDPD	Calculate T_m^* at P^*	i. To benchmark against the experimental surface tension over temperature in combination with Case 2
2	Liquid-vapor (Appendix B)	MDPD	Calculate $\rho^*(T^*)$ and $\gamma^*(T^*)$	ii. To benchmark against the experimental surface tension over temperature in combination with Case 1
3	Water droplet in a vacuum (Appendix C)	MDPD	Calculate water density and surface tension at different droplet sizes	iii. To study the effect of droplet size on density and surface tension droplet iv. To verify the scaling method for water-vapor model
4	Fused silica (Appendix D)	Morse potential	Calculate the mechanical properties of the fused silica	v. To benchmark against the experimental mechanical properties of the fused silica vi. To verify the scaling method for fused silica model
5	Water droplet on a solid substrate (Appendix E)	MDPD, Morse potential, and Lennard-Jones	Calculate contact angles of the liquid-vapor-solid system using different interaction energies between liquid and solid particles	vii. To show the ability to achieve different values of wettability; viii. To verify the scaling method in the solid-liquid-vapor system

$\phi_s = \phi_{lv}^{2/3}$ to maintain the ratios among interfacial energy terms (i.e., solid-vapor, solid-liquid, and liquid-vapor) during scaling, such as

$$\varepsilon'_{sl} = \phi_{lv}^{2/3} \varepsilon_{sl} = \phi_s \varepsilon_{sl}. \quad (25)$$

For the distance parameters σ_{sl} , we assume that Eq. (8) holds, so the scaled σ'_{sl} is calculated as

$$\sigma'_{sl} = 2^{-\frac{1}{6}} \left(\frac{\phi_{lv}^{\frac{1}{3}} r_{mdpd} + \phi_s^{\frac{1}{3}} r_o}{2} \right). \quad (26)$$

This scaling constraint, $\phi_s = \phi_{lv}^{2/3}$, also satisfies automatically the thermal equilibrium condition for different phases. Füchslin *et al.*²² have used $k_b T' = \phi(k_b T)$ for the DPD thermostat because the dissipation-fluctuation relation involves the energy term $k_b T$ (where k_b is the Boltzmann constant). Since a Nosé-Hoover thermostat is used in our model, the scaled temperature parameter used in the Nosé-Hoover thermostats is calculated as $T_{lv}' = \phi_{lv}^{2/3} T_{lv}$ for the liquid-vapor model and

$T_s' = \phi_s T_s$ for the solid model. In the solid-liquid-vapor system, given $\phi_s = \phi_{lv}^{2/3}$ and $T_{lv} = T_s$, we have $T_{lv}' = T_s'$, which satisfies the thermal equilibrium among all phases.

D. Methods of validations and applications

In this study, five cases were used to validate the proposed coarse-grained approach and demonstrate its capability (Table II). The simulations in the first two cases (Case 1 and Case 2) worked together to determine the MDPD parameter B^* for the water-vapor model, as described in Sec. II B. In Case 1, $T_m^*(P^*)$ was calculated using the direct solid-liquid coexistence simulations for MDPD particles. In Case 2, ρ^* and γ^* were calculated using the planar liquid-vapor interface simulation at different temperatures. In Case 3, the simulated density and surface tension were calculated from the water droplet simulation with different droplet sizes, to study the effect of droplet size and quantify the discrepancies from the planar liquid-vapor interface simulation. The scaling method for the water-vapor model was also verified using the results in Case 3. In Case 4, the density, tensile strength, and Young's modulus of the fused silica model were calculated. The tensile strength and Young's modulus were calculated with tensile test simulations at a strain rate of 0.01 s^{-1} . While the minimum strain rate of 0.01 s^{-1} was limited by the computational resources, a number of strain rates were used to study the rate-dependency of the model. The scaling method for the solid model was also verified in Case 4. In Case 5, different values of the wettability of the water-vapor-fused silica system were achieved in the simulations of water droplets on a solid substrate by adjusting different interaction energy between liquid and solid particles.

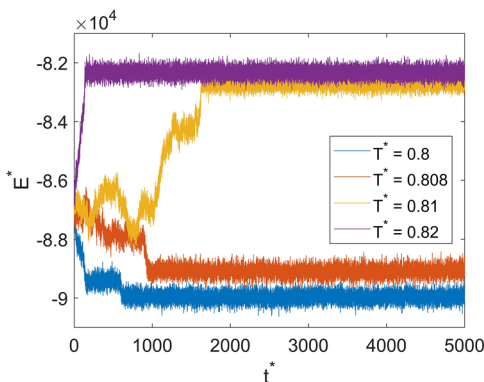


FIG. 2. The total energy of the liquid-solid coexistence simulations evolves with time in the *NPT* ensemble at $P^* = 0$ for $B^* = 50$. The systems at $T^* \geq 0.81$ (the two curves at the top) form liquid and the systems at $T^* \leq 0.808$ (the two curves at the bottom) become solid. The liquid and solid states are determined by plotting the pair distribution function (see Appendix A for more details).

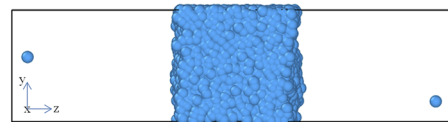


FIG. 3. A snapshot of the liquid film after equilibration for the model with parameters $A^* = -40$, $B^* = 50$, $r_d^* = 0.75$, $r_c^* = 1$ at $T^* = 1$.

TABLE III. The results of the iteration process for $B^* = 50$.

<i>i</i> th iteration	$P_{1\text{atm}}^*$	T_m^*	T_{room}^*	ρ^*	γ^*	$\sigma (\mu\text{m})$	$\epsilon (10^{-12} \text{ J})$	$ T_{i,m}^* - T_{i-1,m}^* /T_{i,m}^* (\%)$
0	0	0.809	0.868	4.862	4.795	16.94	4.351	...
1	113.2	0.945	1.014	4.774	4.26	16.84	4.839	14.39
2	100	0.955	1.025	4.767	4.233	16.83	4.865	1.05
3	99.3	0.957	1.027	0.21

The scaling method for the solid-liquid-vapor system was also verified.

The proposed framework was implemented in LAMMPS.³¹ Snapshots of the simulations were plotted and rendered using Ovito.³⁶ The EAM tabulated files of MDPD potentials [Eq. (5)] were created by using a python code called “atsim.potentials.”³⁷ The Nosé-Hoover chain thermostat was used for temperature control in an isothermal ensemble (constant-temperature, constant-volume NVT ensemble), unless otherwise stated. The pressure control in an isothermal-isobaric ensemble (constant-temperature, constant-pressure NPT ensemble) was achieved with both a Nosé-Hoover chain thermostat and a Parrinello-Rahman barostat.^{13,32,33,38} Unless otherwise stated, the damping parameters for the thermostat and barostat were 100 time steps and 1000 time steps, respectively.

III. RESULTS AND DISCUSSIONS

A. Case 1: Direct liquid-solid coexistence simulation for MDPD

The calculation of T_m^* in the water-vapor model at P^* was carried out by direct liquid-solid interface simulation (details in Appendix A), where the MDPD solid and MDPD liquid were coupled to form a solid-liquid interface and run in the NPT ensemble at the assigned T^* and P^* . Figure 2 shows that the total energy of the system changes with time at different T^* for $B^* = 50$ at $P^* = 0$ as an example. When the solid melts, an increase of the total energy is observed because the thermostat provides extra energy to the system; when liquid freezes, the energy is removed by the thermostat and a decrease of the total energy is observed. The upper and lower limits of the melting temperature $T_{\text{upper}}^* = 0.81$ and $T_{\text{lower}}^* = 0.808$ are found in this case, respectively (Fig. 2). The T_m^* is then calculated as the average of T_{upper}^* and T_{lower}^* , i.e., $T_m^* = 0.809$. The simulations were run using 4394 solid particles. To eliminate the finite size effect, simulations with 2000 and 6750 solid particles were also carried out for $B^* = 50$ at $P^* = 0$, and $T_m^* = 0.809$ was found in all cases. Ultimately, 4394 solid particles have been used in all direct liquid-solid interface simulations.

B. Case 2: Liquid-vapor interface simulation for MDPD

The liquid-vapor interface simulations were performed to calculate the values of $\rho^*(T^*)$ and $\gamma^*(T^*)$ at a given T^* . The

details of the simulations and calculations of $\rho^*(T^*)$ and $\gamma^*(T^*)$ are reported in Appendix B. An example of the equilibrated liquid-vapor simulation is shown in Fig. 3. To calculate T_m^* using the iteration process shown in Table I, $T_m^*(P_{1\text{atm}}^*)$ is calculated based on the simulations in Case 1, while water density $\rho^*(T_{\text{room}}^*(T_m^*))$ and surface tension $\gamma^*(T_{\text{room}}^*(T_m^*))$

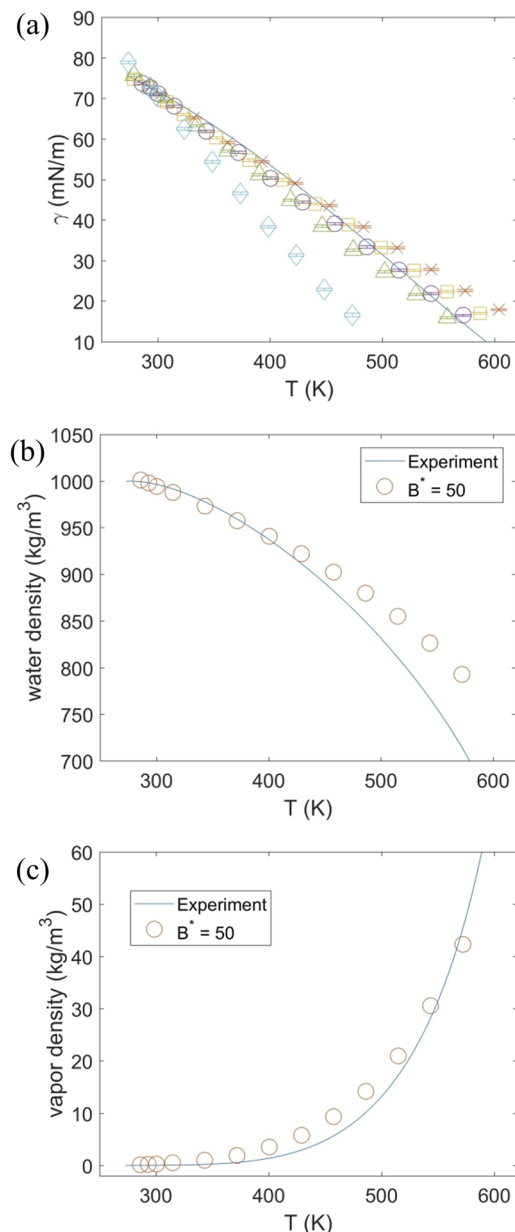
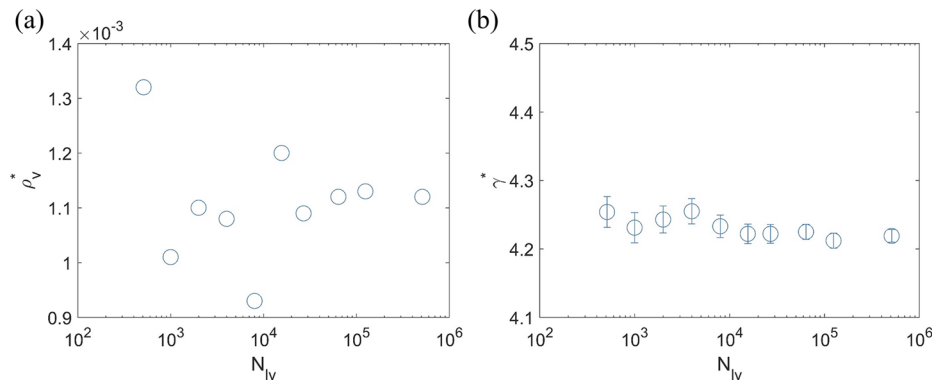


FIG. 4. (a) Surface tension against temperature in dimensional units for $B^* = 48$ (cross), 49 (square), 50 (circle), 51 (triangle), and 60 (diamond); the solid line is the experimental data;³⁹ (b) water density at different temperatures for $B^* = 50$; and (c) the vapor density at different temperatures for $B^* = 50$.

TABLE IV. The calculated T_{room}^* for $B^* = 40, 48, 49, 50, 51$, and 60 .

B^*	48	49	50	51	60
T_{room}^*	0.971	0.999	1.025	1.051	1.177



are calculated here. We have chosen $T_m = 273.15$ K for water to calculate T_{room}^* using Eq. (9). The iteration results for $B^* = 50$ are listed in Table III as an example. The calculation stops at the 3rd iteration, as $|T_{3,m}^* - T_{2,m}^*|/T_{3,m}^* = 0.21\%$. Hence, $T_{2,\text{room}}^* = 1.025$ is chosen as the final room temperature T_{room}^* .

The calculated T_{room}^* values for $B^* = 48, 49, 50, 51$, and 60 are reported in Table IV. The simulated surface tension against the temperature for each B^* is plotted and compared against the experimental surface tension from Ref. 39 [Fig. 4(a)]. The bars in Fig. 4(a) represent the statistical errors of the simulated surface tension, which have been calculated by estimating the statistical inefficiency.^{13,40,41} The best prediction of the experimental surface tension is found for $B^* = 50$ for a temperature in the range of 293 K–600 K. The corresponding fundamental units for $B^* = 50$ are then calculated as $\varepsilon_{\text{mdpd}} = 4.8646 \times 10^{-12}$ J, $\sigma_{\text{mdpd}} = 16.83$ μm , and $m_{\text{mdpd}} = 9.98 \times 10^{-13}$ kg. Figures 4(b) and 4(c) show that the simulation results match the experimental water density up to 450 K and experimental vapor density up to around 600 K. Note that only the simulated water density at the T_{room} has been calibrated against the experimental water density.

The finite size effect of the liquid-vapor simulation was also examined by using different particle numbers N_{lv} at $T_{\text{room}}^* = 1.025$, for $B^* = 50$. The results show that there is no effect of N_{lv} on the liquid density, which is found to be close to constant $\rho_l^* = 4.767$. The vapor density ρ_v^* and surface tension γ^* versus N_{lv} are plotted in Figs. 5(a) and 5(b), respectively. ρ_v^* fluctuates at small N_{lv} and converges to around 0.00112 at $N_{lv} \geq 64\,000$ [Fig. 5(a)]. The values of γ^* are approximately the same for $N_{lv} \geq 8000$ with the error bars overlapping each other [Fig. 5(b)]. Since we are mainly interested in the liquid density and surface tension, this convergence study justifies the use of $N_{lv} = 8000$.

C. Case 3: Water droplet in a vacuum

To study the effect of droplet size on water density and surface tension (Appendix C), water droplets of different sizes were simulated with a different number of particles N_{lv} at $T_{\text{room}}^* = 1.025$ within a box with periodic boundary conditions. Figure 6 shows a snapshot of the droplet simulated with $N_{lv} = 8000$ after equilibration. The droplet is located at the center and the flying particles in the vacuum are the vapor particles. Figures 7(a) and 7(b) show the density and pressure

FIG. 5. (a) Vapor density against the number of particles at $T^* = 1.025$ and (b) surface tension against the number of particles at $T^* = 1.025$.

profiles as a function of the distance r from the center of the simulation box in dimensional units, respectively, for the droplet simulated using different N_{lv} . The profiles start at a distance greater than $1.0 r_c$ in Figs. 7(a) and 7(b) because the local density and pressure have large fluctuations close to the center due to the sampling over small volumes of spherical shell bins (see calculation details in Appendix C). The bulk liquid and vapor densities, i.e., ρ_l^* and ρ_v^* , and bulk pressure in liquid and vapor phases, i.e., P_l^* and P_v^* , are calculated by averaging the data in the bulk region. The corresponding dimensional values calculated with the fundamental units $\varepsilon_{\text{mdpd}} = 4.8646 \times 10^{-12}$ J, $\sigma_{\text{mdpd}} = 16.83$ μm , and $m_{\text{mdpd}} = 9.98 \times 10^{-13}$ kg as $\rho = \rho^* m_{\text{mdpd}} / \sigma_{\text{mdpd}}^3$ and $P = P^* \varepsilon_{\text{mdpd}} / \sigma_{\text{mdpd}}^3$ are listed in Table V.

The error function erf⁴² is found to provide a better fit to our density profile compared to the hyperbolic tangent function,⁴³ and it is used to fit the density profile as a function of r , given ρ_l and ρ_v ,

$$\rho(r) = \frac{1}{2}(\rho_l + \rho_v) - \frac{1}{2}(\rho_l - \rho_v)\text{erf}\left(\frac{\sqrt{\pi}(r - r_{dp})}{w}\right), \quad (27)$$

where r_{dp} and w are the estimated droplet radius and the interface thickness listed in Table V. The value of r_{dp} is close to the equimolar dividing radius r_e , which can be calculated using

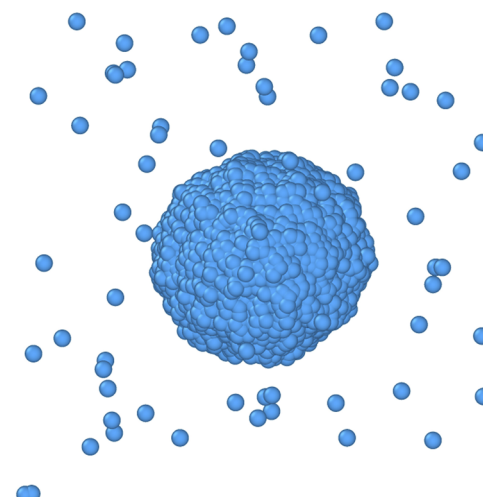


FIG. 6. A snapshot of the simulated water droplet at equilibrium with $N_{lv} = 8000$.

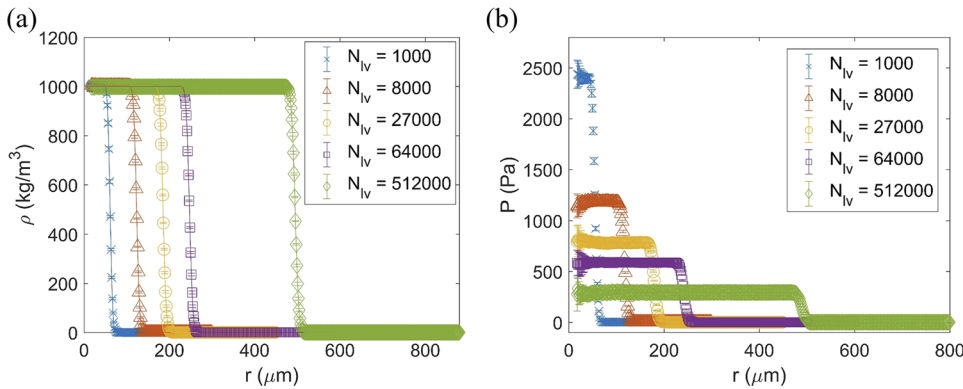


FIG. 7. (a) Density profile against radius r for the simulations with a different number of particles. The solid lines are the fitted density profile using Eq. (27). (b) Pressure profile against radius r for the simulations with a different number of particles. The error bars are calculated from the block averages.

TABLE V. The resulting ρ_l , ρ_v , P_l , P_v , ΔP , r_{dp} , w , and r_e for the droplet simulations with a different particle number N_{lv} .

N_{lv}	ρ_l (kg/m ³)	ρ_v (kg/m ³)	P_l (Pa)	P_v (Pa)	ΔP (Pa)	r_{dp} (μm)	w (μm)	r_e (μm)
512	1011	0.500	3041.3	2.378	3038.9	48.66	11.42	49.16
1 000	1009	0.396	2412.4	1.939	2410.4	61.12	11.99	61.58
4 000	1005	0.333	1500.1	1.623	1498.4	97.60	13.44	97.98
8 000	1003	0.297	1183.8	1.459	1182.4	123.21	14.08	123.55
15 625	1002	0.278	948.3	1.367	946.9	154.22	14.57	154.52
27 000	1002	0.270	783.6	1.327	782.3	185.20	14.9	185.47
64 000	1001	0.266	587.9	1.306	586.6	247.14	15.57	247.38
125 000	1000	0.251	471.2	1.235	470.0	309.10	16.27	309.32
512 000	999	0.253	293.7	1.245	292.4	494.85	17.26	495.04

the following equation:^{13,43}

$$r_e^3 = \frac{1}{\rho_v - \rho_l} \int_0^\infty \frac{d\rho(r)}{dr} r^3 dr, \quad (28)$$

where $\rho(r)$ is as in Eq. (27). The calculated r_e values are listed in Table V. The larger droplet has lower ρ_l and ρ_v ; however, the decrease in ρ_l is small. In addition, the difference in ρ_l between the droplet with $r_e = 123.55$ μm ($N_{lv} = 8000$) and the droplet with largest radius $r_e = 495.04$ μm is around 0.4%. Although the difference in ρ_v between the two droplets (i.e., $r_e = 123.55$ μm and $r_e = 495.04$ μm) is about 18%, the absolute density difference is in fact very small due to the small values of ρ_v .

If the droplet is large enough, the Young-Laplace equation should hold⁴³

$$\Delta P_{YL} = \frac{2\gamma_\infty}{r_e}, \quad (29)$$

where ΔP_{YL} is the pressure difference between the bulk liquid and vapor pressure and γ_∞ is the surface tension at the planar limit. Here, γ_∞ can be obtained from the planar liquid-vapor simulation using the greatest number of particles ($N_{lv} = 512 000$) in Case 2, which is 0.072 46 N/m ($\gamma_\infty^* = 4.219$). To check the validity of Eq. (29) in the droplet simulations, the simulated ΔP (Table V) and the estimated ΔP_{YL} using Eq. (29) at different r_e^{-1} are plotted in Fig. 8. It can be seen from Fig. 8 that ΔP and ΔP_{YL} lie closely together for the droplets with $r_e \geq 97.98$ μm ($N_{lv} \geq 4000$). For those droplets ($r_e \geq 97.98$ μm), a straight line passing through the origin has been fitted to the ΔP at each r_e and its slope is used to estimate the surface tension from droplet simulations (Fig. 8). The

estimated surface tension is 0.0731 N/m, which is within 1% of γ_∞ , demonstrating the validity of Eq. (29) for the droplet with sufficiently large size ($r_e \geq 97.98$ μm).

To verify the scaling method for the water-vapor model, the results of droplet simulations with 27 000, 64 000, 125 000, 512 000 particles are scaled to the same droplet size simulated at $N_{lv} = 8000$ by considering the scaling factors $\phi_{lv} = 8/27, 1/8, 8/125$, and $1/64$, respectively. The fundamental units corresponding to each ϕ_{lv} are calculated using Eqs. (14)–(16). Afterwards, the resulting properties ρ_l , ρ_v , P_l , P_v , and r_e are calculated with the dimensionless values from each

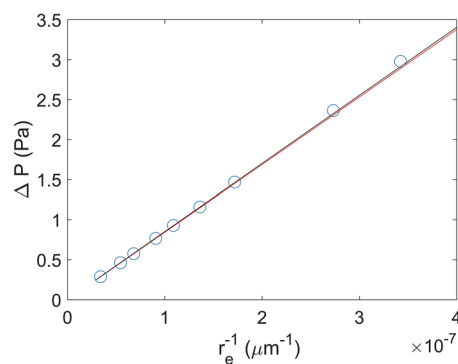
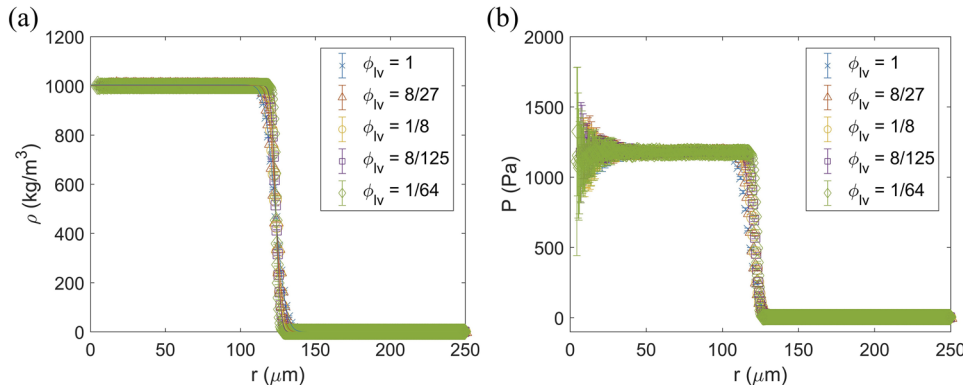


FIG. 8. Pressure difference between liquid and vapor phases against the inverse equimolar dividing radius: the circles are simulation results; the red line is the calculated ΔP_{YL} as in Eq. (29), with $\gamma_\infty = 0.07246$ N/m; the black line is a straight line fitted using the data for $r_e \geq 97.98$ μm and passing through the origin, and it has a slope of 0.1462 N/m and a R-squared value of 0.9999.

TABLE VI. The simulated values of ρ_l , ρ_v , P_l , P_v , ΔP , r_{dp} , w , r_e , and γ for water drops with different scaling factors.

ϕ_{lv}	ρ_l (kg/m ³)	ρ_v (kg/m ³)	P_l (Pa)	P_v (Pa)	ΔP (Pa)	r_{dp} (μm)	w (μm)	r_e (μm)	γ (mN/m)
1	1003	0.297	1183.8	1.459	1182.4	123.21	14.08	123.55	73.04
8/27	1002	0.270	1175.4	1.990	1173.4	123.46	9.93	123.65	72.55
1/8	1001	0.266	1175.8	2.612	1173.2	123.57	7.79	123.69	72.55
8/125	1000	0.251	1178.1	3.087	1175.0	123.64	6.51	123.73	72.69
1/64	999	0.253	1174.8	4.980	1172.7	123.71	4.32	123.76	72.38



case and the corresponding fundamental units (Table VI). Figures 9(a) and 9(b) show the density and pressure profiles in dimensional units for each ϕ_{lv} , respectively. It can be seen from Fig. 9(a) that the width of the interface decreases when ϕ_{lv} decreases. r_e increases slightly with the decrease of ϕ_{lv} as reported in Table VI, but the increment from $\phi_{lv} = 1$ to $\phi_{lv} = 1/64$ is within 0.2%. The change in water density ρ_l is also small from $\phi_{lv} = 1$ to $\phi_{lv} = 1/64$, which is around 0.4%. Since the Young-Laplace equation holds for $N_{lv} \geq 4000$ ($r_e \geq 97.98 \mu\text{m}$), the surface tension of each droplet γ is estimated as $\gamma = \Delta P r_e / 2$ (Table VI). It appears from Table VI that the value of γ at different ϕ_{lv} is close to that at $\phi_{lv} = 1$, and the largest difference in γ is within 1%. With the small changes in ρ_l and γ , we can conclude that the scaling method for the water-vapor model is valid, at least for the tested scaling range.

D. Case 4: Fused silica model

The parameters of the Morse potential model of the fused silica are $D_o = 2.178 \times 10^{-10} \text{ J}$, $r_o = 14.142 \mu\text{m}$, and $\alpha = 51.91 \mu\text{m}^{-1}$ with $m_s = 4.400 \times 10^{-12} \text{ kg}$. The calculation details of density ρ_{sim} , tensile strength f_{sim} , and Young's modulus E_{sim} are reported in Appendix D. In this section, ten tensile test simulations with different initial particle velocity distributions were carried out for a specimen with $N_s = 12\,000$ and an aspect ratio of 1:3 at a strain rate of 0.01 s^{-1} . The averaged f_{sim} and E_{sim} from the 10 results are reported in Table VII. It can be seen from Table VII that the simulated results can match well the corresponding experimental data within the standard deviations. Since the standard deviations of f_{sim} and E_{sim} are small, only one simulation for each case has been carried out for the study of the strain rate effect and verification of the scaling method.

FIG. 9. (a) Density profile against radius r for different scaling factors ϕ_{lv} , and the solid lines are the fitted density profile using Eq. (27); (b) pressure profile against r for different ϕ_{lv} . The error bars are calculated from the block averages.

The stress-strain curves at different strain rates $\dot{\epsilon}$ are shown in Fig. 10(a). The resulting E_{sim} values are 74.16, 73.9, 73.98, and 73.71 GPa, for $\dot{\epsilon} = 0.01, 0.1, 1$, and 10 s^{-1} , respectively. E_{sim} drops slightly with the increase of $\dot{\epsilon}$, while f_{sim} increases with the increase of $\dot{\epsilon}$ [Fig. 10(a)]. Both changes in f_{sim} and E_{sim} are relatively small within the simulated strain rates, suggesting that the results for $\dot{\epsilon} < 0.01 \text{ s}^{-1}$ would not deviate much from the results of the simulation at $\dot{\epsilon} = 0.01 \text{ s}^{-1}$.

To verify the scaling method for the solid model, more tensile test simulations for fused silica with $\phi_s = 8, 1/8$, and $1/64$ were performed at a strain rate of 1 s^{-1} for $N_s = 1500, 96\,000$, and $768\,000$, respectively. The stress-strain curves for different ϕ_s are plotted in Fig. 10(b). The resulting E_{sim} values are 72.67, 73.98, 74.53, and 74.73 GPa, for the $\phi_s = 8, 1, 1/8$, and $1/64$, respectively. The fluctuation of the stress-strain curve for $\phi_s = 8$ is greater than that of the other cases due to the small N_s value used in the simulation, which affects the resulting f_{sim} and E_{sim} values. On the other hand, it seems from Fig. 10(b) that for $\phi_s \leq 1$, f_{sim} is not very sensitive to ϕ_s , while E_{sim} increases slightly with the decrease of ϕ_s . However, these changes are relatively minor as the maximum changes were around 1% for both f_{sim} and E_{sim} . This indicates

TABLE VII. Comparison between the simulation results and targeted experimental values. The value in the parentheses is the standard deviation of the resulting values from the ten simulations.

	ρ (kg/m ³)	E (GPa)	Tensile strength (MPa)
Experimental value	2200	74	69
Simulation result	2200	73.92 (0.219)	69.00 (0.203)

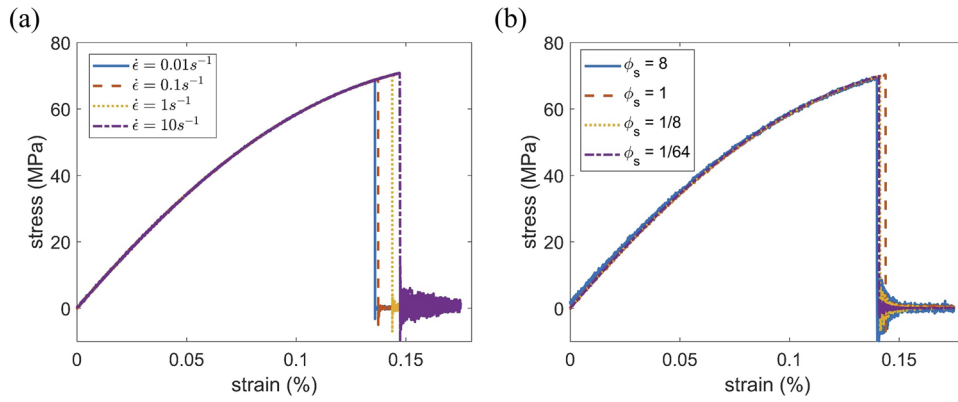
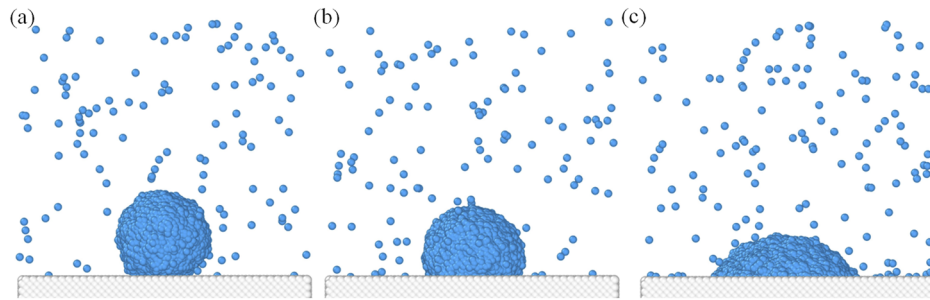


FIG. 10. (a) The stress-strain curves for simulations with $N_s = 12\,000$ at different strain rates; (b) the stress-strain curves for simulations with different scaling factors.



that the proposed scaling method is valid for the solid model with sufficiently large N_s values.

E. Case 5: Water droplet on a solid substrate

To demonstrate the capability of our model in reproducing different degrees of wettability, the contact angles θ of a water droplet on a fused silica substrate were calculated with different interaction energy between liquid and solid particles ($\epsilon_{sl}/\epsilon_{mdpd} = 0.2\text{--}1.4$, see Appendix E for details). Figure 11 shows a snapshot of the simulation after equilibration for different wettability cases. To calculate θ , the 2D density contour is plotted using the averaged local densities of cylindrical shell bins with Matlab [Fig. 12(a)]. The liquid-vapor interface

is determined from the density contour at the location with density ρ_d ,

$$\rho_d = 0.5(\rho_l + \rho_v), \quad (30)$$

where ρ_l and ρ_v are the bulk liquid and vapor densities, which can be obtained from the results of the droplet simulations. To avoid the large perturbations of the liquid density near the substrate, only the liquid-vapor interface $2\sigma_{sl}$ above the substrate is used to fit a circle. An example of fitting a circle to the liquid-vapor interface is shown in Fig. 12(b), and the blue line represents the location of the solid interface. θ is then calculated by determining the tangent line of the circle at the intersection of the circle and the solid interface. Five contact angles have been obtained for each simulation during the production. The averaged value and standard deviation of the five contact angles are then calculated for each case and plotted in Fig. 13.

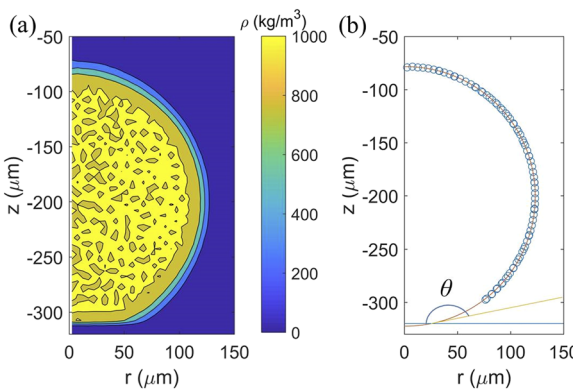


FIG. 12. (a) The density contour for the case of $\epsilon_{sl}/\epsilon_{mdpd} = 0.2$. (b) The circular fit at the liquid-vapor interface for the case of $\epsilon_{sl}/\epsilon_{mdpd} = 0.2$: the hollow dots represent the liquid-vapor interface; the horizontal blue line represents the solid interface; the yellow line is the tangent of the circle at the contact point.

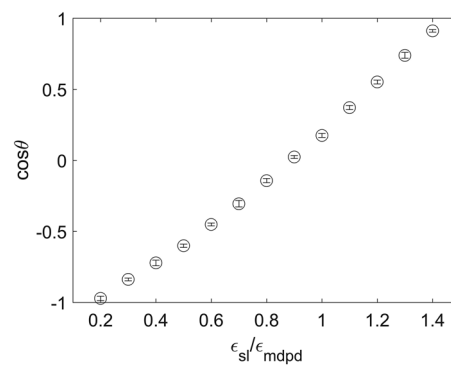


FIG. 13. The cosine of contact angle against the value of $\epsilon_{sl}/\epsilon_{mdpd}$. The error bars are calculated from the standard deviation of cosine of the five contact angles obtained at each simulation and are smaller than the symbol size.

TABLE VIII. The results of the simulated contact angle at different ϕ_{lv} . The standard deviations of the contact angles are listed in the parentheses.

N_{lv}	1000	2197	4096	8000	15 625	64 000
ϕ_{lv}	8	3.641	1.953	1	0.512	0.125
ϕ_s	4	2.367	1.563	1	0.64	0.25
θ (deg)	121.57 (3.17)	124.53 (1.78)	127.32 (1.00)	126.96 (0.81)	127.15 (0.60)	127.33 (0.31)

It can be seen from Fig. 13 that a low ε_{sl} to ε_{mdpd} ratio results in a hydrophobic interaction, while a large ratio leads to a hydrophilic interaction. As a result, the energy parameter of the solid-liquid inter-particle interaction ε_{sl} can be adjusted to reflect the wettability of a liquid on a solid surface. Therefore, ε_{sl} can be calibrated against the desired experimental contact angle. The results of contact angle simulation using different scaling factors ϕ_{lv} for the liquid-vapor particles are listed in Table VIII. The solid substrate with a thickness of three lattice constants was prepared with solid parameters calculated with the scaling factor $\phi_s = \phi_{lv}^{2/3}$. All cases have a simulation domain around $800 \times 800 \times 800 \mu\text{m}^3$. It can be seen from Table VIII that θ converges for $\phi_{lv} \geq 1.95$. For the cases of $\phi_{lv} \leq 3.64$, the discrepancies in the contact angle can be due to using a small number of liquid-vapor particles ($N_{lv} \leq 2197$) since we have shown that the Young-Laplace equation is only valid for the droplet simulations using $N_{lv} \geq 4000$ in Case 3. In summary, the results have validated the scaling method for the solid-liquid-vapor system.

IV. CONCLUSION

In this paper, a coarse-grained MD based framework has been developed for modeling multiphase systems (vapor-liquid-solid) at the microscale. The liquid-liquid/liquid-vapor, solid-solid, and solid-liquid inter-particle interactions are implemented using different potential functions, i.e., MDPD, Morse potential, and Lennard-Jones potential, respectively. As a result, the mechanical properties of the solid and liquid phases emerge from the physical interactions between the particles.

The simulated density and surface tension of the water-vapor model, and the simulated density, tensile strength and Young's modulus properties of the fused silica model were calibrated against experimental data. In particular, the water-vapor model was calibrated against the trend of experimental surface tension of water versus temperature. The experimental water density at a wide range of temperatures (up to 450 K) was also reproduced. It was found from the water-vapor model that the increase of drop size had a minor effect on the water density or the resulting surface tension. For the fused silica model under tension tests, increasing the strain rate could result in a slightly larger tensile strength and slightly smaller Young's modulus. The multiphase interaction simulations were carried out by modeling a water droplet on the solid substrate with different energy parameters of the solid-liquid inter-particle interaction. It was found that there is a clear relation between the energy parameter and the calculated contact angles. Therefore, the solid-liquid inter-particle interaction parameter can

also be calibrated with the experimental contact angle. The modified scaling methods were verified for the liquid-vapor, solid, and solid-liquid-vapor systems. This allows us to model the same system using different particle densities or systems of different sizes using the same particle density, without the need to recalibrate the parameters against experimental data.

The DPD method and its variants have been shown in the literature to successfully model single-phase or multiphase flows at small scale with complex geometric boundaries. However, the assumption of rigid solid is often used in these studies. Our proposed framework includes the explicit modeling of solid-solid interactions, which can be potentially applied to the multiphase simulations involving solid deformation and fracture, such as the crushing of grains in partially saturated porous media under impact. Nonetheless, further development and validation are required for such applications to be fulfilled in future research.

ACKNOWLEDGMENTS

This work was supported in part by the Australian Research Council through Discovery Projects (Nos. DP140100945 and DP170102886), by the National Natural Science Foundation of China (Grant No. 11232003), and by The University of Sydney Nano Institute Postgraduate Top-Up Scholarship. This research was undertaken with the assistance of resources and services from the National Computational Infrastructure (NCI), which is supported by the Australian Government, and the University of Sydney HPC service at The University of Sydney.

APPENDIX A: DIRECT LIQUID-SOLID COEXISTENCE SIMULATION

To determine the melting temperature for water modeled by MDPD, we carried out direct liquid-solid coexistence simulations, which have been applied to molecular dynamics simulations of simple fluids, metal, water, and other types of fluids.⁴⁴ To determine the lattice structure for the MDPD solid, an isothermal-isobaric cooling process was performed from high temperature to low temperature and the BCC structure for the solid was found after solidification. Therefore, a BCC-structure solid system was prepared with 4394 particles and a size of $13 \times 13 \times 13$ lattice constants. The system was equilibrated in the NPT ensemble for 100 000 steps, at the assigned P^* and a T^* close to the melting temperature. The method of direct liquid-solid coexistence simulations used here was similar to the method of García Fernández *et al.*⁴⁵ for water models. The time step size for the MDPD model was

$\Delta\tau^* = 0.001$. The liquid system was prepared and relaxed in the *NVT* ensemble for 100 000 steps to have the same volume and temperature as the solid system so that the two systems can be combined. The particle numbers used in the liquid system were estimated with the equilibrium density calculated from the simulation of bulk liquid phase in the same *NPT* ensemble conditions of the solid system. Next, the liquid and solid systems were combined, and a short run (10 000 time steps) was performed to relax the interfacial stress between the two phases. During this relaxation, only the liquid particles were allowed to move with a Langevin thermostat to prevent the solid from melting due to a large amount of energy generated at the interface. After the relaxation, the initial velocities of the particles were drawn from Gaussian distribution and adjusted to have zero total linear and angular momenta. The system was then run in the anisotropic *NPT* ensemble with a given P^* but varying T^* values. The anisotropic *NPT* ensemble allows each length of simulation box to change independently to meet the desired pressure in each direction. If the solid melts, it indicates that T^* is greater than T_m^* . If the liquid solidifies, then T^* is smaller than T_m^* . The liquid or solid state of the system was determined using the pair distribution function. The total energy of the system was monitored to capture melting or solidifying phenomena.⁴⁵ The melting temperature was calculated as the average of the upper and lower limits at the given P^* .

The liquid or solid state of the system can be determined using the pair distribution function with OVITO.³⁶ An example of pair distribution functions plotted at $P^* = 0$ and $B^* = 50$ for both liquid ($T^* = 0.81$) and solid ($T^* = 0.808$) states is shown in Fig. 14, corresponding to the plot of total energy against time in Fig. 1. As we can see from Fig. 2, the total energy of the system reaches an equilibrium after around 1600 t^* for $T^* = 0.81$ and drops to an equilibrium just before around 1000 t^* for $T^* = 0.808$. The pair distribution functions are then plotted at a time after the system is equilibrated: at 1000 t^* for $T^* = 0.81$ and at 1800 t^* for $T^* = 0.81$. One can see that the pair distribution function changes from its initial state (liquid-solid coexistence) to liquid state for $T^* = 0.81$, as the function for $T^* = 0.81$ tends to fluctuate around 1 after the first sharp peak (Fig. 14). The pair distribution function of the solid state has slightly greater maximum values at the peaks and smaller minimum values at the valleys of

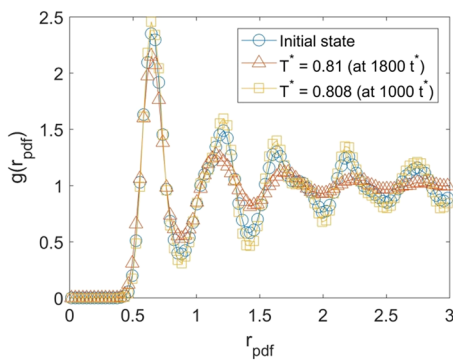


FIG. 14. Pair distribution functions for $P^* = 0$ and $B^* = 50$ at the initial state (beginning of the simulation), $T^* = 0.81$ (at 1800 t^*), and $T^* = 0.808$ (at 1000 t^*).

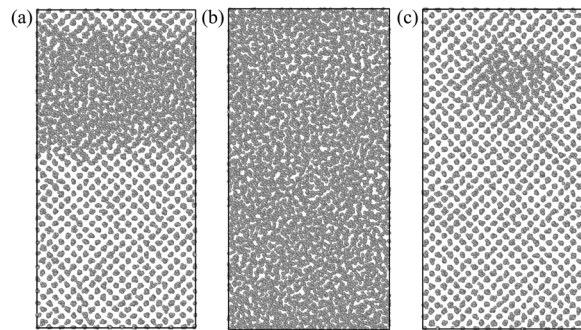


FIG. 15. The diagram shows the particles in the y - z plane for (a) the initial state (solid-liquid coexistence), (b) the liquid state for $T^* = 0.81$ at 1800 t^* , and (c) the solid state for $T^* = 0.808$ at 1000 t^* . The particle radius of 0.1 is used to plot the figures for the purpose of visualization. The length is not to scale, as L_z changes under the anisotropic *NPT* ensemble during the simulation.

the functions, as compared to the function of the initial solid-liquid coexistence (Fig. 14). Another method to determine the liquid and solid states is to plot the snapshot of the simulations. The initial particle coordinates, the particle coordinates obtained from the simulations for $T^* = 0.808$ at 1000 t^* and for $T^* = 0.81$ at 1800 t^* are plotted in Fig. 15. It can be seen that the system becomes solid for $T^* = 0.808$ [Fig. 15(c)] and becomes liquid for $T^* = 0.81$ [Fig. 15(b)]. It is noted that a small amount of particles does not turn into solid structures, as this may be due to the boundary effects of the rectangular cell.

APPENDIX B: LIQUID-VAPOR INTERFACE SIMULATION

To calculate the bulk density and surface tension of water at a specific temperature T^* , the liquid-vapor interface simulation was performed. We first created 8000 particles in a cubic simulation box with a density not far away from the equilibrium density. This 8000-particle system represented a microscale computational domain of $200 \times 200 \times 200 \mu\text{m}^3$ with periodic boundary conditions. The experimental water density at room temperature was 998 kg/m^3 . Hence, the mass per particle $m_{\text{mdpd}} = 9.98 \times 10^{-13} \text{ kg}$ was calculated from Eq. (10). The number of molecules per particle was estimated as $m_{\text{mdpd}}/m_{\text{water}} = 3.336 \times 10^{13}$, where m_{water} is the mass of one water molecule. The time step $\Delta\tau^* = 0.001$ was selected to satisfy the criterion of energy conservation for the equilibrated liquid system running in a microcanonical constant-energy, constant-volume (NVE) ensemble: the root-mean-square (RMS) fluctuation of the total energy had to be less than 10% of the RMS fluctuation of kinetic energy.^{46,47} The cubic water system was equilibrated through a 500 000 step run in the *NPT* ensemble at the assigned T^* and $P^* = 0$. The initial particle velocities were drawn from a Gaussian distribution so as to have temperature T^* and were adjusted to result in zero total linear and angular momenta. After the bulk water system was equilibrated, a liquid film with two planar interfaces was created by expanding the simulation box length in the z -direction by a factor 4. The *NPT* ensemble was then switched to the *NVT* ensemble for an isothermal simulation with a fixed volume. The simulation was run for 2 000 000 steps for equilibration and for another 4 000 000 steps for

production. Equilibrium of the system was verified when the total energy fluctuated around a constant value. For the simulation running at high T^* , it took a longer time to equilibrate. Using 2 000 000 steps was adequate for all the liquid-vapor interface simulations considered in this work. To calculate the density profile, the simulation box was divided into slab bins with a width of $0.2 r_c^*$ in the z-direction, and the local density in each bin was calculated at every $20 \Delta\tau^*$. The density profile along the z-axis was computed from the time-averaged density in each bin and was used to calculate the bulk liquid and vapor densities. The density profile would drift slightly during the simulation along the z-direction, especially at high T^* . To better compute the liquid and vapor densities, for the system running at $T^* > 1.2$, the center of mass of the system was kept at the center of the box by shifting the positions of particles. This was achieved by modifying the LAMMPS code. The surface tension γ was calculated every $20 \Delta\tau^*$ using the following equation:⁴⁸

$$\gamma = \frac{1}{2}L_z < P_{zz} - \frac{P_{xx} + P_{yy}}{2} >, \quad (\text{B1})$$

where P_{xx} , P_{yy} , and P_{zz} are the virial pressure components and L_z is the length of the box in the z-direction. The statistical errors of the surface tension were estimated by calculating the statistical inefficiency.^{13,40,41}

APPENDIX C: WATER DROPLET IN VACUUM SIMULATION

The water droplets of different sizes in dimensionless units were simulated by varying the number of particles, namely, $N_{\text{lv}} = 512, 1000, 4000, 8000, 15\,625, 27\,000, 64\,000, 125\,000$, and $512\,000$. The parameters of $A^* = -40$, $B^* = 50$, $r_c^* = 1$, and $r_d^* = 0.75$ were used. To model the droplet, the initial configurations of the relaxed bulk liquid were taken from the size-effect studies of liquid-vapor interface simulations, in which the system had been equilibrated in the *NPT* ensemble at $T^* = 1.025$ and $P^* = 0$ for 500 000 time steps with periodic boundary conditions being applied to all faces. The lengths of the simulation box in all three directions were then extended by a factor of 3 so that water could have enough space to evolve into a spherical droplet. Random velocities generated with a Gaussian distribution at the temperature $T^* = 1.025$ were then assigned to the particles and adjusted to have zero total linear and angular momentum for the system. The system was run in the *NVT* ensemble for 6×10^6 steps. The first 2×10^6 steps were considered for equilibration, and the last 4×10^6 steps were considered for production, except for the simulation with $N_{\text{lv}} = 512\,000$. The simulation with $N_{\text{lv}} = 512\,000$ took longer to equilibrate; hence, 4×10^6 steps of equilibration and 2×10^6 steps of production were used. The center-of-mass of water particles was fixed at the center of the simulation box by shifting the coordinates of the particles at every time step. To obtain the local density as a function of the radial distance from the center of the simulation box, the simulation box was divided into a set of spherical shell bins with a thickness of $0.1\sigma_{\text{mdpd}}^*$ and an origin from the center of the box. The normal pressure component was calculated from the Irving-Kirkwood pressure tensor,⁴⁹ by following the details of calculation

presented in Ref. 43. A modified LAMMPS was used to perform such a calculation. The local density and pressure were computed every 20 steps averaged during production. The bulk density and pressure in liquid and vapor phases were obtained by averaging the corresponding data within the bulk region.⁵⁰ Since the spherical shell bins have smaller volumes approaching to the center, only small numbers of particles were sampled in the shell bins close to the center. Hence, large fluctuations of the density and pressure profiles occurred over the region close to the center of the droplet, the data in such a region were not used in the calculation of the bulk liquid density and pressure.⁴³ The standard deviations were calculated from the block averages. There were 20 blocks in total for $N_{\text{lv}} \leq 125\,000$ and 10 blocks for $N_{\text{lv}} = 512\,000$ and each block contained 10 000 configurations.

APPENDIX D: FUSED SILICA SIMULATIONS

The calculation of density, tensile strength, and Young's modulus for fused silica is presented in this section. After a few simulations using the trial and error method, the final parameters were found as $m_s = 4.400 \times 10^{-12}$ kg, $D_o = 2.178 \times 10^{-10}$ J, $r_o = 14.142 \mu\text{m}$, and $\alpha = 51.91 \mu\text{m}^{-1}$. For calculation of the density, 4000 CG particles in the FCC structure were created in a simulation box with periodic boundary conditions, representing the $200 \times 200 \times 200 \mu\text{m}^3$ fused silica. For the given parameters, each particle was mainly influenced by their nearest neighbor particles so that a relatively small cutoff radius $r_{\text{ss,cut}} = 1.1 r_o$ was used. The damping parameters for the thermostat and the barostat were $100 \Delta\tau$ and $10\,000 \Delta\tau$, respectively, where $\Delta\tau$ was the time step. $\Delta\tau = 0.5$ ns was selected so that the ratio of the root-mean-square fluctuation of the total energy to the root-mean-square fluctuation of kinetic energy was less than 10%, for the equilibrated simulations running in the *NVE* ensemble.^{46,47} The system was first run in the *NPT* ensemble for 50 000 steps for equilibration with $P = 0$ and T calculated from the room temperature of the water model. Afterwards, a production run of 50 000 steps was performed, during which the density was calculated.

To perform the tensile test, a $200 \times 200 \times 600 \mu\text{m}^3$ specimen was constructed using 12 000 particles in the simulation box with a periodic boundary condition applied in the loading direction (z-axis). The system was equilibrated at a zero pressure along the z-axis ($P_z = 0$) and T calculated from the room temperature of the water model for 500 000 steps. The length of the equilibrated specimen in the z-direction is recorded as L_o . Engineering strain was calculated as $(L - L_o)/L_o$. After equilibration, the specimen was stretched in the z-direction at a constant strain rate of 0.01 s^{-1} until it fractured. This strain rate was limited by the computational resources. During the displacement controlled loading, a Nosé-Hoover chain thermostat was used to control the temperature. To accurately represent the bulk properties and minimize the surface effects, the stresses of the inner center group of the particles within the initial region of $140 \times 140 \times 420 \mu\text{m}^3$ were calculated every 100 000 steps (Fig. 16). The virial stress tensor of the i th particle in LAMMPS was calculated as the negative value of the pressure tensor,⁵¹

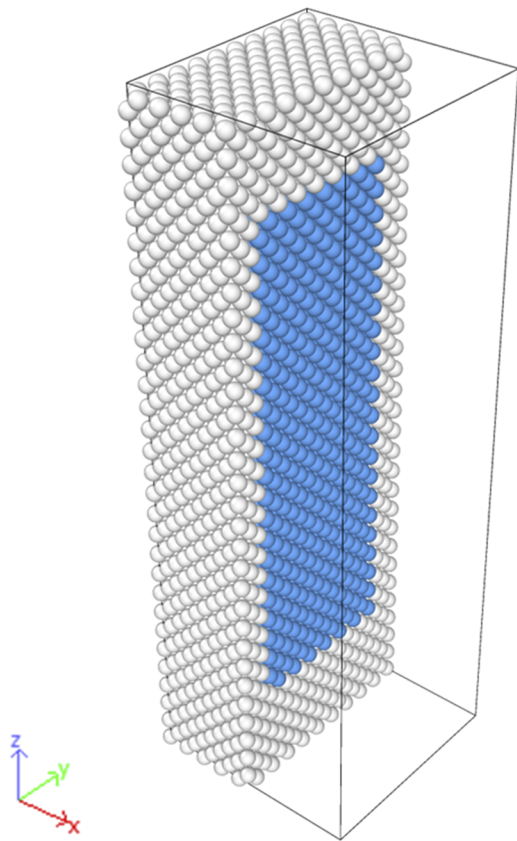


FIG. 16. The stress is calculated from the blue particles inside of the specimen in the initial region of $140 \times 140 \times 420 \mu\text{m}^3$. Only half of the specimen is shown.

$$S_{i,pq} = -\frac{1}{V_i} [m_i v_{i,p} v_{i,q} + \frac{1}{2} \sum_j^{N_p} (r_{i,p} F_{i,q} + r_{j,p} F_{j,q})], \quad (\text{D1})$$

where p and q are the indices for tensor components (e.g., values for x, y, and z), m_i and v_i are the mass and velocity of the i th particle, F_i is the force on the i th particle due to its j th neighbor particle, and the summation is taken over all the neighbor particles N_p of the i th particle. The volume of the i th particle V_i in this group was calculated from Voronoi tessellation using Voro++.^{52,53} There were around 3000 data points for the stress-strain curve from the beginning of loading to failure. The simulated tensile strength f_{sim} was calculated as the maximum value of the calculated stress. The simulated Young's modulus E_{sim} was calculated as the slope of the line that best fits the data points within the first 10% of the failure strain. In addition to the strain rate $\dot{\epsilon} = 0.01 \text{ s}^{-1}$, the simulations under $\dot{\epsilon} = 0.1, 1, \text{ and } 10 \text{ s}^{-1}$ were also performed. The stress and strain data were obtained at every 10 000, 1000, and 100 time steps for $\dot{\epsilon} = 0.1, 1, \text{ and } 10 \text{ s}^{-1}$, respectively, to have around 3000 data points from the beginning of loading to failure. The tensile test simulations were also performed for different scaling factors: $\phi_s = 8, 1/8 \text{ and } 1/64$, at a strain rate of 1 s^{-1} . Here the simulation using $N_s = 12000$ corresponded to the case of $\phi_s = 1$. Thus, we used $N_s = 1500, 96000 \text{ and } 768000$ for the simulations with $\phi_s = 8, 1/8 \text{ and } 1/64$, respectively. The parameters for $\phi_s = 8, 1/8 \text{ and } 1/64$ were calculated using Eqs. (21)–(24) with the current parameters of the fused silica model.

APPENDIX E: SIMULATIONS OF DROPLETS ON A SOLID SUBSTRATE

The liquid-vapor-solid simulation was demonstrated by modeling a liquid droplet on a solid substrate. The calibrated MDPD parameters of the water-vapor model in Case 2 and the Morse potential parameters of the fused silica model in Case 4 were used for modeling a droplet and a solid substrate, respectively. A time step of 0.5 ns was used, as taken from the minimum value of the time steps used in the above two models. An $800 \times 800 \times 800 \mu\text{m}^3$ simulation box with periodic boundary conditions was created. The FCC solid substrate was created in the x-y plane of the box with a thickness of 3 lattice constant ($a_s = 20 \mu\text{m}$) using 22 400 particles. A cube of 8000 water particles was then placed above the solid substrate. To adjust the energy interaction between the liquid and solid particles, the ratio of ε_{sl} to $\varepsilon_{\text{mdpd}}$ was changed from 0.2 to 1.4. The σ_{sl} value in the LJ potential function was estimated using Eq. (8): $\sigma_{\text{sl}} = 2^{-\frac{1}{6}} \left(\frac{r_{\text{mdpd}} + r_o}{2} \right)$. The location of the minimum energy in MDPD potentials r_{mdpd} was estimated from the first peak of the pair distribution function for liquid at room temperature under zero pressure, which was $10.948 \mu\text{m}$, and $r_o = 14.142 \mu\text{m}$ from the fused silica parameters was used. Therefore, σ_{sl} was calculated as $11.176 \mu\text{m}$. A cutoff radius of $3\sigma_{\text{sl}}$ was used. Two *NVT* ensembles were applied individually to the water-vapor particles and solid particles with the same temperature damping parameter of $100 \Delta\tau$, except for the bottom layer of the substrate, which was fixed to constrain the center of mass of the entire solid substrate. In addition, the center-of-mass velocity of the droplet was removed for the temperature calculation of the water-vapor particles used in the Nosé-Hoover chain thermostat. Each simulation was run for 50×10^6 steps. The first 30×10^6 steps were for equilibration and the following 20×10^6 steps were for production. During the production, the coordinates of the entire system were shifted every time step to ensure that the x- and y-coordinates of the center-of-mass of the water-vapor particles were fixed at the center of the simulation box. This is to make sure that the center-of-mass of the droplet in the x- and y-directions would not deviate much from the center, given the small amount of vapor particles in the system. To plot the 2-D density contour, the simulation box was divided into cylindrical shell bins with an origin at the center of the box, a radial thickness of $5 \mu\text{m}$, and a height thickness of $5 \mu\text{m}$. The density profile was recorded every 1000 time steps and averaged at every 4×10^6 steps during production. Each density profile was used to calculate the contact angle. The mean contact angle was calculated by averaging five contact angles and the uncertainty was estimated by calculating the standard deviation. The same calculations were applied to the cosine of the contact angle. To check the validity of the scaling method in the solid-liquid-vapor system, the liquid-vapor particles were scaled with the liquid-vapor scaling factor ϕ_{lv} . The number of liquid-vapor particles N_{lv}' were then created based on $N_{\text{lv}}' = N_{\text{lv}}/\phi_{\text{lv}}$, while the solid particles were created with a thickness of three lattice constants and an area of around $800 \times 800 \mu\text{m}^2$. The scaled liquid-vapor particle mass was calculated using Eq. (14) and the parameters of liquid-vapor particles were calculated with ϕ_{lv} using Eqs. (17)–(20). The particle mass and parameters

of the solid particles were calculated with the solid scaling factor $\phi_s = \phi_{lv}^{2/3}$ using Eqs. (21)–(24). The parameters of interaction between solid and liquid-vapor particles (Lennard-Jones potential) were calculated using Eqs. (25) and (26). The sizes of the simulation box were also simulated at around $800 \times 800 \times 800 \mu\text{m}^3$ for each case.

- ¹B. E. Martin, W. Chen, B. Song, and S. A. Akers, *Mech. Mater.* **41**, 786 (2009).
- ²M. Omidvar, M. Iskander, and S. Bless, *Int. J. Impact Eng.* **49**, 192 (2012).
- ³S. Wang, L. Shen, F. Maggi, A. El-Zein, and G. D. Nguyen, *Int. J. Impact Eng.* **102**, 156 (2017).
- ⁴S. Wang, L. Shen, F. Maggi, A. El-Zein, G. D. Nguyen, Y. Zheng, H. Zhang, and Z. Chen, *Int. J. Impact Eng.* **116**, 65 (2018).
- ⁵J. Ghorbani, M. Nazem, and J. Carter, *Comput. Geotech.* **71**, 195 (2016).
- ⁶B. Shahbodagh-Khan, N. Khalili, and G. A. Esgandani, *Comput. Geotech.* **69**, 411 (2015).
- ⁷R. Uzuoka and R. I. Borja, *Int. J. Numer. Anal. Methods Geomech.* **36**, 1535 (2012).
- ⁸B. K. Cook, D. R. Noble, and J. R. Williams, *Eng. Comput.* **21**, 151 (2004).
- ⁹M. Liu, P. Meakin, and H. Huang, *Water Resour. Res.* **43**, W04411, <https://doi.org/10.1029/2006wr004856> (2007).
- ¹⁰L. Li, L. Shen, G. D. Nguyen, A. El-Zein, and F. Maggi, “A smoothed particle hydrodynamics framework for modelling multiphase interactions at meso-scale,” *Comput. Mech.* (published online).
- ¹¹H. Huang, P. Meakin, and M. Liu, *Water Resour. Res.* **41**, W12413, <https://doi.org/10.1029/2005wr004204> (2005).
- ¹²L. Jing, C. Kwok, Y. Leung, and Y. Sobral, *Int. J. Numer. Anal. Methods Geomech.* **40**, 62 (2016).
- ¹³M. P. Allen and D. J. Tildesley, *Computer Simulation of Liquids* (Oxford University Press, New York, 1987).
- ¹⁴S. Izvekov and G. A. Voth, *J. Phys. Chem. B* **109**, 2469 (2005).
- ¹⁵D. Reith, M. Pütz, and F. Müller - Platthe, *J. Comput. Chem.* **24**, 1624 (2003).
- ¹⁶H.-J. Qian, P. Carbone, X. Chen, H. A. Karimi-Varzaneh, C. C. Liew, and F. Müller-Plathe, *Macromolecules* **41**, 9919 (2008).
- ¹⁷S. J. Marrink, A. H. De Vries, and A. E. Mark, *J. Phys. Chem. B* **108**, 750 (2004).
- ¹⁸S.-W. Chiu, H. L. Scott, and E. Jakobsson, *J. Chem. Theory Comput.* **6**, 851 (2010).
- ¹⁹O. Lobanova, C. Avendaño, T. Lafitte, E. A. Müller, and G. Jackson, *Mol. Phys.* **113**, 1228 (2015).
- ²⁰M. Arrienti, W. Pan, X. Li, and G. Karniadakis, *J. Chem. Phys.* **134**, 204114 (2011).
- ²¹A. Kumar, Y. Asako, E. Abu-Nada, M. Krafczyk, and M. Faghri, *Microfluid. Nanofluid.* **7**, 467 (2009).
- ²²R. M. Füchslin, H. Fellermann, A. Eriksson, and H.-J. Ziock, *J. Chem. Phys.* **130**, 214102 (2009).
- ²³R. D. Groot and P. B. Warren, *J. Chem. Phys.* **107**, 4423 (1997).
- ²⁴I. Pagonabarraga and D. Frenkel, *J. Chem. Phys.* **115**, 5015 (2001).
- ²⁵P. Warren, *Phys. Rev. E* **68**, 066702 (2003).
- ²⁶A. Ghoufi and P. Malfreyt, *Phys. Rev. E* **83**, 051601 (2011).
- ²⁷F. Goujon, A. Dequidt, A. Ghoufi, and P. Malfreyt, *J. Chem. Theory Comput.* **14**, 2644 (2018).
- ²⁸C. Chen, L. Zhuang, X. Li, J. Dong, and J. Lu, *Langmuir* **28**, 1330 (2011).
- ²⁹Z. Li, G.-H. Hu, Z.-L. Wang, Y.-B. Ma, and Z.-W. Zhou, *Phys. Fluids* **25**, 072103 (2013).
- ³⁰A. Ghoufi, J. Emile, and P. Malfreyt, *Eur. Phys. J. E* **36**, 10 (2013).
- ³¹S. Plimpton, *J. Comput. Phys.* **117**, 1 (1995).
- ³²D. Frenkel and B. Smit, *Understanding Molecular Simulation: From Algorithms to Applications* (Academic Press, San Diego, 2001).
- ³³W. Shinoda, M. Shiga, and M. Mikami, *Phys. Rev. B* **69**, 134103 (2004).
- ³⁴M. S. Daw and M. I. Baskes, *Phys. Rev. B* **29**, 6443 (1984).
- ³⁵S. J. Schneider, *Engineered Materials Handbook, Volume 4: Ceramics and Glasses* (ASM International, USA, 1991).
- ³⁶A. Stukowski, *Modell. Simul. Mater. Sci. Eng.* **18**, 015012 (2009).
- ³⁷M. Rushton, <http://atsim potentials.readthedocs.io/en/latest/> (accessed April 14, 2016).
- ³⁸G. J. Martyna, D. J. Tobias, and M. L. Klein, *J. Chem. Phys.* **101**, 4177 (1994).
- ³⁹NIST Chemistry WebBook, NIST Standard Reference Database Number 69, edited by P. J. Linstrom and W. G. Mallard (National Institute of Standards and Technology, Gaithersburg, 2017) (retrieved April 19, 2017).
- ⁴⁰R. Friedberg and J. E. Cameron, *J. Chem. Phys.* **52**, 6049 (1970).
- ⁴¹D. Fincham, N. Quirk, and D. Tildesley, *J. Chem. Phys.* **84**, 4535 (1986).
- ⁴²S. Arcidiacono, D. Poulikakos, and Y. Ventikos, *Phys. Rev. E* **70**, 011505 (2004).
- ⁴³S. Thompson, K. Gubbins, J. Walton, R. Chantry, and J. Rowlinson, *J. Chem. Phys.* **81**, 530 (1984).
- ⁴⁴C. Vega, E. Sanz, J. Abascal, and E. Noya, *J. Phys.: Condens. Matter* **20**, 153101 (2008).
- ⁴⁵R. García Fernández, J. L. Abascal, and C. Vega, *J. Chem. Phys.* **124**, 144506 (2006).
- ⁴⁶W. Van Gunsteren and H. Berendsen, *Mol. Phys.* **34**, 1311 (1977).
- ⁴⁷H. Berendsen, and W. Van Gunsteren, *Molecular Liquids* (Springer, 1984), p. 475.
- ⁴⁸A. E. Ismail, G. S. Grest, and M. J. Stevens, *J. Chem. Phys.* **125**, 014702 (2006).
- ⁴⁹J. Irving and J. G. Kirkwood, *J. Chem. Phys.* **18**, 817 (1950).
- ⁵⁰M. Nijmeijer, C. Bruin, A. Van Woerkom, A. Bakker, and J. Van Leeuwen, *J. Chem. Phys.* **96**, 565 (1992).
- ⁵¹A. P. Thompson, S. J. Plimpton, and W. Mattson, *J. Chem. Phys.* **131**, 154107 (2009).
- ⁵²C. H. Rycroft, G. S. Grest, J. W. Landry, and M. Z. Bazant, *Phys. Rev. E* **74**, 021306 (2006).
- ⁵³C. H. Rycroft, “Voro++: A three-dimensional voronoi cell library in C++,” Paper LBNL-1430E, Lawrence Berkeley National Laboratory, 2009.